

Integrated Sensing and Communication System Based on Radio Frequency Resonance Beam

Yixuan Guo, Shuaifan Xia, Mingliang Xiong, Qingwen Liu, *Senior Member, IEEE*, Shengli Zhou, *Fellow, IEEE*, Wen Fang, Qingwei Jiang, Gang Yan, *Member, IEEE* and Jiangchuan Mu

Abstract—To address the challenge of complex beam control in traditional multiple-input multiple-output (MIMO) systems, research has proposed establishing adaptive beam alignment by utilizing retro-directive antenna (RDA) arrays to create echo resonance between the base station (BS) and user equipment (UE), thereby reducing system computational load. However, in conventional resonant beam systems (RBS), the use of the same frequency for uplink and downlink inevitably leads to echo interference issues. Therefore, this paper proposes an innovative design for an resonance beam-based integrated sensing and communication (RB-ISAC) system to achieve efficient passive sensing and bidirectional communication. In this system, the UE does not actively transmit signals but instead relies on a passive phase conjugation and frequency conversion structure to separate the uplink and downlink carrier frequencies. Additionally, through effective compensation for signal propagation loss, resonance is achieved after multiple iterations, at which point the beam's field distribution becomes a low-diffraction-loss, high-focusing pattern, automatically aligning the transmitter with the receiver. This enables high-precision passive positioning while facilitating uplink and downlink communication. Simulation results demonstrate that the proposed system can achieve resonance after multiple iterations, and can support uplink and downlink communication within a range of 5 meters while achieving passive direction of arrival (DOA) estimation with an error of less than 2 degrees.

Index Terms—Passive ISAC, resonant beam system, retro-directive antenna, MIMO, beamforming, direction of arrival, frequency division system.

I. INTRODUCTION

WITH the rapid development of wireless communication and intelligent technologies, the increasing demand for emerging applications such as the internet of things (IoT), vehicle-to-everything (V2X), and drone swarms not only requires high communication throughput but also precise localization to ensure the normal operation of the equipments [1]. Single-function systems are no longer sufficient to meet the dual demands of high-precision localization and efficient communication [2], [3]. Consequently, integrated sensing and communication (ISAC) systems have gradually become an

Y. Guo and J. Mu is with the Shanghai Research Institute for Intelligent Autonomous Systems, Tongji University, Shanghai 201210, China (e-mail: {guoyixuan, jiangchuan_mu}@tongji.edu.cn).

S. Xia, W. Fang, Q. Jiang and Q. Liu is with the College of Electronics and Information Engineering, Tongji University, Shanghai 201804, China (e-mail: {collinxia, wen.fang, jiangqw, qliu}@tongji.edu.cn).

M. Xiong is with the Department of Computer Science and Technology, Tongji University, Shanghai 201804, China (email: mlx@tongji.edu.cn).

S. Zhou is with the Department of Electrical and Computer Engineering, University of Connecticut, Storrs, CT 06269, USA (email:shengli.zhou@uconn.edu).

G. Yan is with the School of Physics Science and Engineering, Tongji University, Shanghai 200092, China (e-mail: gyan@tongji.edu.cn).

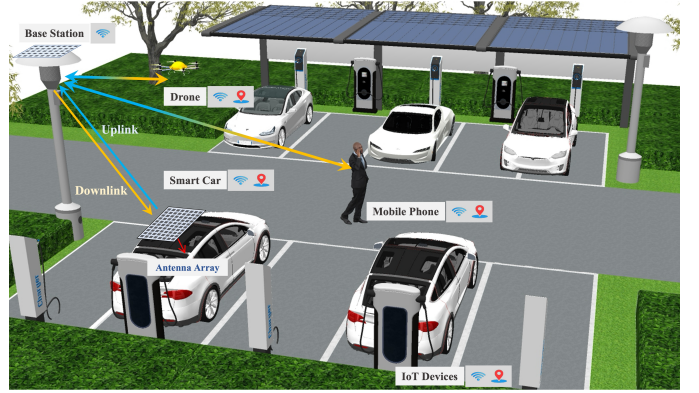


Fig. 1. Simultaneous localization and communication systems are used in smart parking lots, with downlink communication and uplink for localization.

essential component of future wireless networks [4], [5]. Integrating localization and communication functions effectively to achieve resource sharing and collaborative optimization holds significant practical importance and broad application prospects. Fig. 1 illustrates a typical application scenario in a smart parking lot, where the base station (BS) can provide communication services to IoT devices within the area and simultaneously obtain their location information, even for passive devices that are incapable of actively transmitting signals.

Millimeter-wave (mmWave) networks, as a wireless network technology capable of supporting dynamic scenarios and diverse applications, have gained significant attention in recent years [6]. Due to the much higher propagation loss of mmWave compared to lower frequency bands, beamforming (BF) techniques are required to focus signal power, thereby extending propagation paths and improving communication performance. Some researchers have explored the optimization of mmWave BF matrices through learning-based methods to enhance network quality [7]. However, in large-scale multiple-input multiple-output (MIMO) systems, the training overhead caused by a large number of antenna elements poses a major challenge. To address this issue, some researchers have investigated the feasibility of installing sensors in the infrastructure to support mmWave communication, further reducing training complexity [8]. Beyond the communication domain, mmWave technology has also shown great potential in localization systems. Leveraging its ultra-wideband characteristics and large-scale antenna arrays, mmWave enables high-precision and highly robust localization, primarily benefiting from the

inverse relationship between antenna size and beamwidth [9], [10], [11], [12].

However, most current studies still focus on either communication or localization tasks individually, rather than addressing the ISAC scenarios. For applications requiring both high-efficiency communication and high-precision localization, there is an urgent need for a unified and efficient framework. The authors of [13], [14] investigated the joint transceiver design for ISAC systems. The authors of [15] explored the applications of ISAC in intelligent transportation, and the authors of [16] examined the communication resource allocation problem in drones-assisted ISAC scenarios.

It is evident that designing ISAC systems in the millimeter-wave band faces multiple challenges. Firstly, under limited wireless resources, the core issue is how to simultaneously achieve high localization accuracy and high communication rates. Secondly, the complexity of beamforming also places higher demands on system design. In traditional communication systems, beamforming is primarily used to direct signal power to the receiver to optimize communication efficiency [17]. However, in ISAC systems, beamforming not only serves the communication function but also directly affects localization accuracy [18]. Therefore, reducing the complexity of beamforming control is critical, especially in large-scale MIMO systems.

In the optical frequency band, numerous studies have demonstrated that resonant beam systems (RBS) possess adaptive beam alignment characteristics. By installing two optical retro-reflective devices at the transmitting and receiving ends and allowing the laser to oscillate back and forth multiple times, waves of the same frequency and phase can superimpose, while waves with different phases gradually attenuate until they cancel out. This enables strongly directional BF without the need for channel estimation and beam control [19], [20], [21], [22]. Furthermore, existing research has confirmed that migrating RBS to the mmWave band can continue to retain these advantages, achieving high-precision passive localization [23] and highly efficient wireless power transfer [24]. However, the RBS structure based on single-frequency round-trip propagation will generate echo interference when supporting communication. Since the uplink and downlink signals are transmitted on the same frequency, the reflected and retransmitted signals inevitably interfere with each other. This interference becomes particularly severe after multiple round trips, significantly degrading the demodulation quality of communication signals. To address this issue, [25] proposed a frequency-division-based RBS, in which the BS establishes uplink and downlink frequency-divided channels upon receiving signals from the UE. However, this system is not suitable for passive localization.

Based on the above research, we further integrated mmWave localization technology into the frequency-division RBS system and propose a resonant beam-based integrate sensing and communication (RB-ISAC) system. The proposed system not only effectively resolves the interference issue between uplink and downlink signals but also fully leverages the high-resolution characteristics of the millimeter-wave band. Without requiring the UE to actively transmit signals, the system adaptively achieves simultaneous localization and communication, pro-

viding a simpler solution for passive ISAC applications in the mmWave band.

The main contributions of this paper are as follows.

- To address the beamforming complexity in existing mmWave ISAC systems, we propose an RB-ISAC system. Frequency division between uplink and downlink is realized using the phase-locked loops (PLL). Without the need for additional complex algorithmic controls, the system achieves adaptive formation of uplink and downlink links through signal recovery and enhancement mechanisms as well as frequency adjustment, significantly reducing implementation complexity.
- To solve the interference problem between uplink and downlink signals in traditional single-frequency round-trip RBS systems, we design a frequency-division passive localization scheme. This scheme overcomes the inability of radio frequency-based resonate beam passive localization systems to support communication. By separating the frequencies of uplink and downlink signals, it ensures power transmission efficiency while achieving high-quality signal transmission and high-precision passive localization.
- To validate the feasibility of the proposed system, an RB-ISAC analytical model is constructed. This model theoretically analyzes the conditions for achieving resonance and quantitatively evaluates communication quality and localization performance. Simulation results demonstrate that the proposed system exhibits excellent performance in both passive communication quality and localization accuracy, providing critical design guidance for practical deployment.

The remainder of this paper is organized as follows. Section II introduces the system structure design of the RB-ISAC and the principle of resonance formation. Section III provides a detailed mathematical analysis model, including the power circulation model of the RB-ISAC system, the communication channel model, and the direction of arrival (DOA) estimation method. Section IV presents the simulation results and their analysis, covering the resonance formation process, convergence analysis, communication quality evaluation, and DOA accuracy assessment. Finally, Section V summarizes the research findings of this paper.

II. SYSTEM DESIGN

In this section, we first present the system structure design of the PLL-based retro-directive antenna (RDA) array to achieve frequency separation for the uplink and downlink, ensuring that the initial phase of the output signal matches the phase of the received signal. Subsequently, by adjusting the spacing between array elements, we ensure that the output signal can accurately point toward the signal source. Additionally, we explain the principle of achieving resonance in the RB-ISAC system.

A. The Principle of Frequency Division in RB-ISAC

The RB-ISAC system consists of a BS and UE. The BS and UE transmit and receive signals through planar arrays composed of M and N RDAs, respectively. Fig. 2 illustrates the system

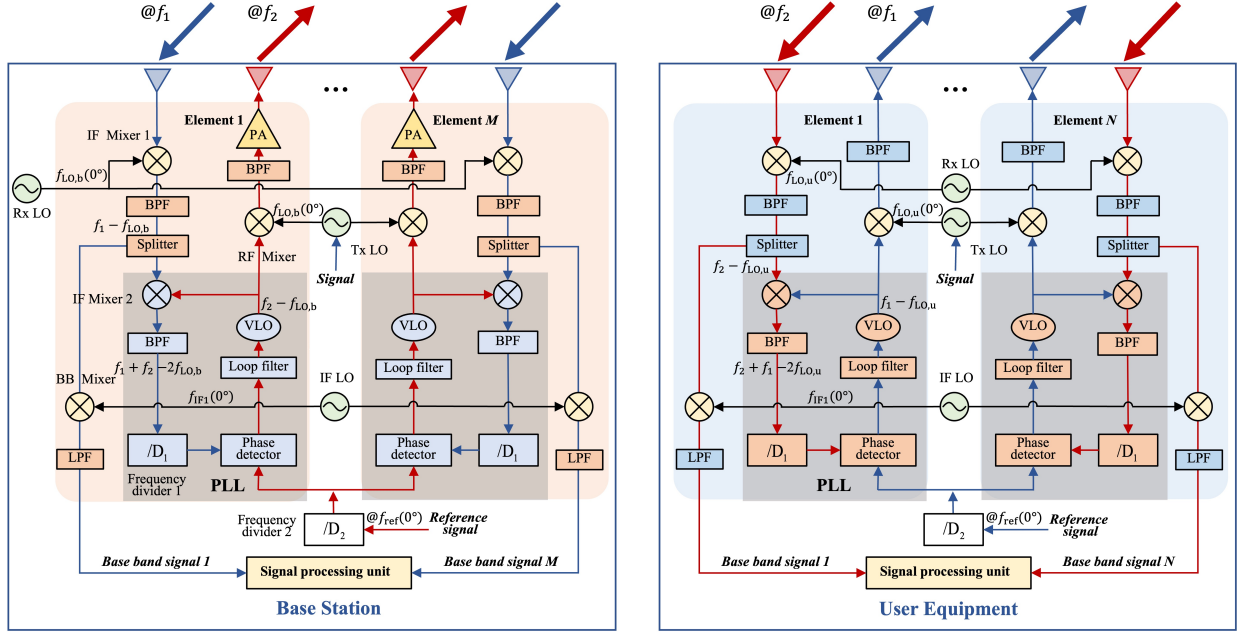


Fig. 2. Diagram of uplink and downlink frequency separation structure and conjugate circuit structure in resonant beam-based integrated localization and communication system.

structure based on the RDA array. We assume that the UE is semi-passive [26], meaning that although it is equipped with an RDA array, the UE does not need to actively transmit signals. Initially, the BS spatially broadcasts an electromagnetic wave with frequency f_2 . When the UE, also equipped with an RDA array, receives the signal, it reflects the signal with frequency f_1 back to the BS.

The BS initially radiates electromagnetic waves into space. When the UE, also equipped with an RDA array, receives the signal, it reflects the signal back to the BS. The receiving (Rx) antenna of the BS first captures the RF signal, which is then down-converted using an intermediate frequency (IF) mixer in combination with a local oscillator (LO) signal $f_{LO,b}$. During this process, the output signal generated by the mixer passes through a band-pass filter (BPF), retaining the intermediate frequency component $f_{IF1} = f_1 - f_{LO,b}$.

Subsequently, the signal is directed through a power splitter, with one portion of the intermediate frequency signal routed to a base band (BB) mixer. This signal is mixed with a LO signal at frequency f_{IF} . After passing through a low-pass filter (LPF) to remove high-frequency components, the resulting base band signal is fed into the signal processing unit (SPU) for further processing and analysis.

The remaining signal enters frequency divider 1 in the phase-locked loop (PLL) for D_1 -fold frequency division. It is then compared with a reference signal that has undergone D_2 -fold frequency division in the phase detector, generating a phase error signal. This error signal is a voltage signal proportional to the phase difference. A loop filter is used to remove high-frequency noise and unwanted fluctuations, resulting in a smooth DC control voltage that adjusts the frequency of the voltage-controlled oscillator (VCO) [27].

At this point, the VCO generates an IF signal locked to the phase of its input signal, with a frequency of $f_2 - f_{LO}$. This

signal is up-converted using IF Mixer 2, where it is mixed with the IF signal f_{IF1} input to the PLL. This generates a new IF signal with a frequency of

$$f_{IF2} = f_1 + f_2 - 2f_{LO,b}. \quad (1)$$

The resulting IF signal re-enters the PLL loop for frequency and phase adjustments until the phase of the received input signal matches the phase of the PLL output signal, i.e., the phase error becomes zero [28], [29]. At this point, the PLL achieves phase locking and the locked signal is sent to the RF mixer. In the RF mixer, the signal is mixed with the transmitting (Tx) LO signal, which carries modulation information, and up-converted to the RF band f_2 . Finally, the signal is passed through a BPF to remove spurious frequencies, amplified, and transmitted as an RF signal.

At this point, the relationship between the frequencies and phases of the PLL's input and output signals can be expressed as

$$\frac{f_{ref}}{D_2} = \frac{f_1 + f_2 - 2f_{LO,b}}{D_1}, \quad (2)$$

$$\frac{\phi_{ref}}{D_2} = \frac{\phi_1 + \phi_2 - 2\phi_{LO,b} + 2n\pi}{D_1}. \quad (3)$$

here, f_{ref} and ϕ_{ref} are the frequency and phase of the reference signal, respectively. Assuming that both the LO signal and the reference signal have a phase of 0° , we can derive

$$f_2 = \frac{D_1}{D_2} f_{ref} + 2f_{LO,b} - f_1, \quad (4)$$

$$\phi_2 = -\phi_1. \quad (5)$$

From this, it can be seen that the signal successfully undergoes frequency conversion and achieves phase conjugation

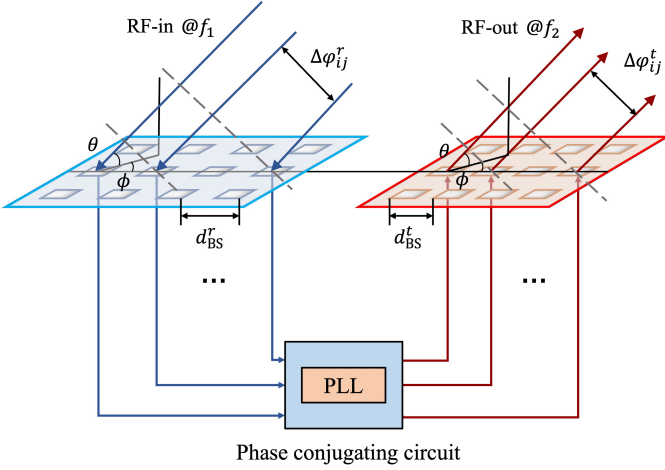


Fig. 3. Schematic diagram of the principle of RB-ISAC echo signal original path return.

after processing through the system. This ensures that the output signal frequency meets the specified conditions, while the output signal phase becomes the conjugate of the input signal phase [30].

Here, we provide an example design. For example, one can set $f_1 = 31$ GHz and $f_{LO,b} = 28$ GHz, which leads to $f_{IF1} = 3$ GHz, while $f_2 = 29$ GHz, then the frequency of the VCO output signal is 1 GHz, and $f_{IF2} = 4$ GHz. When the reference signal frequency $f_{ref} = 1$ GHz, frequency divisions can be set to $D_1 = 4$ and $D_2 = 1$. Different from the design of [25], where the PLL recovers the frequency of the received signal, and then mixes it with the frequency of the modulated signal to generate a new frequency, the PLL in RB-ISAC can achieve frequency conversion.

The operation of the UE's antenna is similar to that of the BS. However, the BS must be equipped with a power amplifier to boost the output signal power, compensating for signal losses during transmission and ensuring that the downlink signal is strong enough to reach the UE. Additionally, the BS's signal processing unit needs to analyze the phase of the received signal to obtain the DOA information of the UE, while the UE does not require this capability.

B. Dual Frequency Resonance Principle

As mentioned above, both the BS and UE can recover the phase of the transmitted signal through the RDA arrays. However, due to the change in frequency, if only the initial phase is controlled, the transmitted signal and the received signal will inevitably not be parallel. Therefore, to ensure the directivity of the signal, improvements to the array are necessary. As shown in Fig. 3, the phase difference between the i -th element and j -th element in the BS's Rx array can be expressed as

$$\Delta\varphi_{ij}^r = \frac{2\pi}{\lambda_1} D_{ij}^r, \quad (6)$$

where λ_1 is the wavelength of the carrier signal with frequency f_1 , and D_{ij}^r denotes the distance between the i -th and j -th

element of the Rx array. It can be represented by DOA as

$$D_{ij}^r = i \cdot d_{BS}^r \sin \theta \cos \phi + j \cdot d_{BS}^r \sin \theta \cos \phi, \quad (7)$$

where d_{BS}^r is the Rx element spacing, θ is the elevation angle, and ϕ is the azimuth angle. To ensure the signal output by the BS can be redirected back to the UE, the output signal's azimuth and elevation angles must match those of the received signal, i.e., $\Delta\varphi_{ij}^t = \Delta\varphi_{ij}^r$.

According to eq.6, the spacing between the elements of the Tx array and the Rx array should satisfy

$$\frac{D_{ij}^r}{D_{ij}^t} = \frac{f_1}{f_2}. \quad (8)$$

The phase-conjugated signal with frequency f_2 can be generated and redirected to the UE [31], [32]. The RDA array on the UE side follows a similar process.

The BS and UE ensure the parallelism of the downlink and uplink by processing the phase of the received signal through conjugation and frequency separation. Specifically, the BS utilizes the conjugate phase information of the received signal to adjust the direction of the transmitted beam, precisely pointing it toward the location of the UE. On the UE side, the RDAs processes the received signal in the same manner through conjugation and frequency division, and then reflects the signal back to the BS. Through this iterative back-and-forth process, electromagnetic waves in space form a standing wave pattern along a specific path, achieving beam self-alignment between the BS and UE.

III. ANALYTICAL MODEL

In this section, we first establish a downlink and uplink signal transmission circulation model for the RB-ISAC system and analyze the conditions for the system to reach a steady state. Then, the channel model of the proposed system is presented, including the expressions for downlink and uplink signals. Finally, we estimate the DOA of the BS received signal using the MUSIC algorithm.

A. Power Circulation Model

In the RB-ISAC system, signal transmission and efficiency are crucial for signal enhancement and closed-loop signal transmission in the uplink and downlink. Specifically, the UE does not need to actively transmit signals. The BS initially radiates electromagnetic waves with a central frequency of f_2 into space. Upon receiving the signal from the BS, the RDA array of the UE uses a LO and a mixer to return the electromagnetic waves to the BS at a central frequency of f_1 . The power density of the uplink signal received by the m -th antenna on the BS plane can be expressed as

$$W_{BS,m}^r = \sum_{n=1}^N \frac{1}{4\pi} P_{UE,n}^t G_{UE,n} l_{nm}^{-\alpha}, \quad (9)$$

where $P_{UE,n}^t$ and $G_{UE,n}$ represent the transmitted power and antenna gain of the n -th antenna of the UE, respectively. l_{nm} is the distance between the m -th antenna on the BS and the n -th antenna on the UE, and α is the path loss exponent.

According to electromagnetic wave theory [33], the time-averaged power density per unit area can be represented using the Poynting vector

$$W = \frac{1}{2} \vec{E} \cdot \vec{H}, \quad (10)$$

where \vec{E} and \vec{H} are the electric field intensity and magnetic field intensity, respectively. In free space or a uniform medium, the relationship between the electric field and the magnetic field is $\vec{H} = \vec{E}/\eta$, where η is the characteristic impedance (wave impedance) of the medium. Therefore

$$W = \frac{|\vec{E}|^2}{2\eta}. \quad (11)$$

Thus, the electric field intensity of the electromagnetic wave radiated from the UE to the BS can be expressed as

$$E_{BS,m}^r = \sum_{n=1}^N \sqrt{\frac{\eta}{2\pi} P_{UE,n}^t G_{UE,m} l_{nm}^{-\alpha} e^{j\Delta\phi_{nm}}}, \quad (12)$$

where $\Delta\phi_{nm} = k_1 l_{nm}$ represents the phase difference of the signal transmitted from the n -th antenna of the UE to the m -th antenna of the BS, $k_1 = 2\pi/\lambda_1$ is the wavenumber of the uplink electromagnetic wave, and λ_1 is the wavelength corresponding to the central frequency f_1 .

The signal power received by the BS is determined by the effective reception area of the antenna and the signal intensity on the BS surface

$$\begin{aligned} P_{BS}^r &= \frac{G_{BS,m} \lambda_1^2}{8\pi\eta} (E_{BS}^r)^2 \\ &= \frac{\lambda_1^2}{16\pi^2} \sum_{m=1}^M \sum_{n=1}^N \left| \sqrt{P_{UE,n}^t G_{UE,n} G_{BS,m} l_{nm}^{-\alpha} e^{j\Delta\phi_{nm}}} \right|^2, \end{aligned} \quad (13)$$

where $G_{BS,m}$ is the gain of the m -th antenna on the BS.

After receiving the signal from the UE, the BS extracts the necessary signals for localization and communication through a signal processing module. The remaining signal power is amplified to a predetermined gain to compensate for the unavoidable power loss during propagation. The signal frequency is then converted to f_2 , and the signal undergoes phase conjugation through the RDAs before being retransmitted to the UE, achieving bidirectional transmission. The actual transmitted signal power from the BS can be expressed as

$$P_{BS}^t = f_A \{ (1 - \beta_{\text{com}} - \beta_{\text{loc}}) \cdot \text{conj}(P_{BS}^r) \}, \quad (14)$$

where β_{com} represents the proportion of the received signal power at the BS used for communication, β_{loc} represents the proportion used for localization, and $\text{conj}(\cdot)$ is denote the phase conjugation operation. It is important to note that the amplification function here represents the power gain for each array element, rather than applying a fixed amplification factor for each element, as the latter would be detrimental to beamforming.

After retransmission, the downlink signal power received by the UE is

$$P_{UE}^r = \frac{\lambda_2^2}{16\pi^2} \sum_{m=1}^M \sum_{n=1}^N \left| \sqrt{P_{BS,m}^t G_{UE,n} G_{BS,m} l_{nm}^{-\alpha} e^{j\Delta\phi_{nm}}} \right|^2. \quad (15)$$

It should be noted that even if the uplink and downlink link lengths are the same, the phase differences may not necessarily match due to the difference in carrier frequencies. The downlink transmission efficiency at this moment can be defined as

$$\mu_{\text{DL}} = \frac{P_{UE}^r}{P_{BS}^t}. \quad (16)$$

When the UE receives the electromagnetic waves from the BS, not all the received power is directly utilized for uplink signal transmission. A portion of the power is allocated to the signal processing module to extract the communication-required information, as well as to support the basic operation of the device, such as frequency conversion and signal processing functions. The remaining power is adjusted to the uplink frequency and then returned to the BS via phase-conjugated operations, expressed as

$$P_{UE}^t = f_A \{ (1 - \gamma_{\text{com}} - \gamma_{\text{wok}}) \cdot \text{conj}(P_{UE}^r) \}, \quad (17)$$

where γ_{com} denotes the proportion of the received signal power used for communication, and γ_{wok} denotes the proportion allocated to support the basic operation of the device.

During the k -th iteration, the power loss of the RB-ISAC system can be represented as

$$\begin{aligned} \mathbf{P}_{BS}^{t,k} - \mathbf{P}_{BS}^{r,k+1} &= \mathbf{P}_{BS}^{t,k} - (1 - \gamma_{\text{com}} - \gamma_{\text{wok}}) \mu_{\text{UL}} \mathbf{P}_{UE}^{r,k} \\ &= \mathbf{P}_{BS}^{t,k} - (1 - \gamma_{\text{com}} - \gamma_{\text{wok}}) \mu_{\text{UL}} \mu_{\text{DL}} \mathbf{P}_{BS}^{t,k}, \end{aligned} \quad (18)$$

where $\mathbf{P}_{BS}^{t,k}$ and $\mathbf{P}_{BS}^{r,k}$ represent the transmitted and received signal powers of the BS during the k -th iteration, respectively, and $\mathbf{P}_{UE}^{r,k}$ represents the signal power transmitted by the UE during the k -th iteration.

Similarly, at the beginning of the $(k+1)$ -th iteration, the power gain of the BS's amplifiers for each antenna can be expressed as

$$\mathbf{P}_{BS}^{t,k+1} - \mathbf{P}_{BS}^{r,k+1} = \mathbf{P}_{BS}^{t,k+1} - (1 - \gamma_{\text{com}} - \gamma_{\text{wok}}) \mu_{\text{UL}} \mu_{\text{DL}} \mathbf{P}_{BS}^{t,k}. \quad (19)$$

From (18) and (19), it can be observed that when k is relatively small, the gain must exceed the loss to ensure the quality of signals in the uplink and downlink transmission process. When the number of iterations reaches a certain value, (18) and (19) become equal, RB-ISAC achieves a steady state. At this point, the amplifier compensates for the propagation loss of electromagnetic waves in a single iteration, and the system reaches its optimal state. The power efficiency also achieves its peak, and the power transmitted and received by the BS converges to a constant value. The electric field distribution becomes stable, which is beneficial for passive localization as the received signal strength remains stable and directionality is evident.

B. Channel Model

In wireless communication systems, accurate channel modeling is a crucial step in analyzing and optimizing system performance. In the RB-ISAC system, the BS and UE generate communication carriers embedded with information through modulators and radiate them via RDA arrays. The downlink carrier signal radiated by the m -th BS can be expressed as

$$S_{BS,m}^t = \sqrt{2\eta P_{BS,m}^t} e^{j(2\pi f_2 t + \phi_m)}, \quad (20)$$

The downlink carrier signal is emitted by the BS antenna array, where each antenna element independently radiates into space with a unique phase ϕ_m and covers the entire space. The received effective carrier signal matrix by the UE from the BS can be expressed as

$$\mathbf{S}_{\text{UE}}^r = \mathbf{H}_{\text{DL}} \mathbf{S}_{\text{BS}}^t + \mathbf{n}, \mathbf{S}_{\text{UE}}^r \in \mathbb{C}^{N \times 1}, \quad (21)$$

where $\mathbf{S}_{\text{BS}}^t \in \mathbb{C}^{M \times 1}$ is the transmission matrix of the BS, and $\mathbf{n} \in \mathbb{C}^{N \times 1}$ is the additive white Gaussian noise (AWGN) which variance $\sigma_{\text{DL}}^2 = 2\eta\kappa T B_{\text{DL}}$ and it is uniformly distributed and independently and identically distributed (i.i.d.), κ is the Boltzmann constant, and $\kappa = 1.38 \times 10^{-23}$ J/K, T is the ambient temperature, and B_{DL} is the downlink carrier bandwidth [34]. $\mathbf{H}_{\text{DL}} \in \mathbb{C}^{N \times M}$ is the channel gain matrix composed of channel gains between different elements of UE and BS, and the downlink channel gain h_{DL}^{mn} can be expressed as

$$h_{\text{DL}}^{mn} = \frac{\lambda_2}{4\pi} \sqrt{G_{\text{UE},n} G_{\text{BS},m} l_{mn}^{-\alpha}} e^{j\Delta\phi_{mn}}, \quad (22)$$

where λ_2 is the wavelength corresponding to the downlink carrier frequency, $G_{\text{UE},n}$ and $G_{\text{BS},m}$ are the gains of the UE and BS antennas, respectively, l_{mn} is the distance between the m -th BS antenna and the n -th UE antenna, and α is the path loss exponent [24], [35].

After receiving the signal from the BS, the UE generates a signal through PLL to recover the phase of the downlink signal for uplink transmission.

Then, the uplink base band signal of the n -th UE antenna is modulated onto the carrier signal, and its frequency is converted to f_1 via an RF mixer, generating the final uplink transmission carrier signal from the UE. This signal can be mathematically expressed as

$$S_{\text{UE},n}^t = \sqrt{2\eta P_{\text{UE},n}^t} e^{j(2\pi f_1 t + \phi_n)}. \quad (23)$$

This marks the end of one iterative cycle. The signal-to-noise ratio (SNR) of the downlink signal received at the RDA of UE is defined as the ratio of the total received signal power used for communication to the noise power, which can be expressed as

$$\text{SNR}_{\text{DL}} = \frac{\gamma_{\text{com}} P_{\text{UE}}^t}{2\eta\kappa T B_{\text{DL}}}. \quad (24)$$

Assuming both BS and UE have perfect channel state information (CSI), the maximum achievable total data rate for the downlink carrier can be expressed as

$$R_{\text{DL}} = B_{\text{DL}} \log_2 (1 + \text{SNR}_{\text{DL}}). \quad (25)$$

On the other hand, spectral efficiency (SE) is another critical metric for evaluating the performance of a communication system. SE reflects the average number of bits transmitted per unit of bandwidth, providing a direct indication of the system's ability to transfer information within limited spectral resources. It is a key parameter in the design and optimization of communication systems and can be expressed as

$$\zeta_{\text{DL}} = \frac{R_{\text{DL}}}{B_{\text{DL}}} = \log_2 \left(1 + 10^{0.1(\text{SNR}_{\text{DL}} - \mathcal{L})} \right), \quad (26)$$

where the \mathcal{L} is the channel loss. Combining with (25), it is evident that higher power transfer efficiency contributes to

maximizing the system's communication performance under limited bandwidth resources. It is noteworthy that quantization noise causes SNR saturation, thereby limiting the maximum value of spectral efficiency [36].

C. DOA Estimation

In the RB-ISAC system, DOA estimation is a critical step for achieving spatial localization and beamforming. By analyzing the signal distribution characteristics on the receiving antenna array, the location of the signal source relative to the array center can be inferred. This process typically involves the construction of the array signal model and the application of high-resolution DOA estimation algorithms. This section provides a detailed analysis of the processing of signals received by the BS from the UE and discusses the principles of DOA estimation using the MUSIC algorithm. After receiving the reflected pass-band signal from the UE, the BS downconverts it to a base band signal by mixing it with the LO signal using the IF mixer. A portion of this signal is then directed to the SPU for DOA estimation. For analytical convenience, the SPU received base band signal matrix can be expressed as

$$\mathbf{S}_{\text{loc}} = \sqrt{\beta_{\text{loc}}} \mathbf{a}(\theta, \phi) \mathbf{S}_{\text{UE}}^t + \mathbf{n}, \quad (27)$$

where $\mathbf{S}_{\text{loc}} \in \mathbb{C}^{M \times 1}$ represents the SPU received signal vector of BS, encompassing signals from all array elements. The vector \mathbf{a} is the steering vector of the UE array center point, expressed as

$$\mathbf{a}(\theta, \phi) = \text{vec}(\mathbf{a}_x(\theta, \phi) \otimes \mathbf{a}_y(\theta, \phi)), \quad (28)$$

where the steering vectors in the x and y directions can be further represented as

$$\mathbf{a}_x(\theta, \phi) = [1 \exp\{jkd \sin \theta \cos \phi\} \dots \exp\{jk(\sqrt{M}-1)d \sin \theta \cos \phi\}]^T, \quad (29)$$

$$\mathbf{a}_y(\theta, \phi) = [1 \exp\{jkd \sin \theta \sin \phi\} \dots \exp\{jk(\sqrt{M}-1)d \sin \theta \sin \phi\}]^T. \quad (30)$$

By employing array signal processing techniques, such as the MUSIC algorithm, and utilizing the orthogonality between the signal vector and the noise vector, the position of the signal source relative to the receiving array center can be inferred. First, the covariance of the received signal at the BS can be calculated as

$$\begin{aligned} R_r &= \mathbb{E}[\mathbf{S}_{\text{loc}} \mathbf{S}_{\text{loc}}^H] \\ &= \mathbf{a} \mathbb{E}[\mathbf{S}_{\text{UE}}^t \mathbf{S}_{\text{UE}}^{tH}] \mathbf{a}^H + \mathbb{E}[\mathbf{nn}^H] \\ &= \mathbf{a} R_s \mathbf{a}^H + R_n. \end{aligned} \quad (31)$$

Assuming that the noise is a zero-mean complex Gaussian random variable, its covariance matrix can be expressed as $R_n = \sigma_{\text{UL}}^2 I$. Based on the covariance matrix R_r , eigenvalue decomposition can be performed to obtain the signal subspace and the noise subspace

$$R_r = U_s \Lambda_s U_s^H + U_n \Lambda_n U_n^H, \quad (32)$$

where $U_s \in \mathbb{C}^{M \times 1}$ represents the signal subspace of the BS received signal, containing the eigenvectors corresponding to

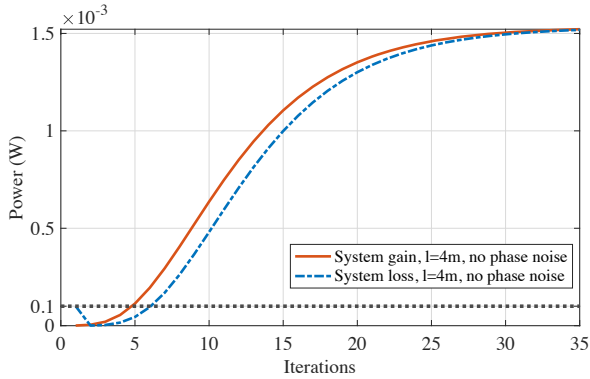


Fig. 4. The process of system loss and gain changing with iteration.

the signal, and $U_n \in \mathbb{C}^{M \times (M-1)}$ represents the noise subspace, containing the $M - 1$ noise eigenvectors. Λ represents the diagonal matrix of eigenvalues.

The fundamental assumption of the MUSIC algorithm is that the steering vector corresponding to the signal direction is orthogonal to the noise subspace. For the true DOA, this relationship satisfies

$$\mathbf{a}^H U_n = 0. \quad (33)$$

Based on this property, MUSIC constructs a spectral function

$$P_{\text{MUSIC}}(\theta, \phi) = \|U_n^H \mathbf{a}(\theta, \phi)\|^{-2}, \quad (34)$$

where $U_n^H \mathbf{a}(\theta, \phi)$ represents the projection of the steering vector onto the noise subspace. By searching for the peaks of the MUSIC spectrum, the DOA information of the UE can be estimated.

IV. PERFORMANCE EVALUATION

In this section, we conduct a simulation analysis of the system performance for the dual-frequency RB-ISAC. First, we illustrate the process by which the system achieves resonance through iterations. Then, we evaluate the communication metrics of the system, including transmission efficiency, SNR, and SE. Finally, we analyze the accuracy of the system's passive DOA estimation. Table I provides the parameters used in the simulation.

A. Establishment of Resonance

We present the variation of system gain and system loss with respect to the number of iterations in Fig. 4. For a more intuitive observation, phase noise is not considered here. According to eq. (18) and eq. (19), the system reaches a steady state when the gain and loss within one iteration cycle effectively cancel each other out. As shown in the Fig. 4, at the beginning of the iteration process, the system loss is greater than the gain. This is because, during the first iteration, the BS radiates electromagnetic waves with a total omnidirectional power of 0.1 mW, but the actual power received at the UE is relatively low. Therefore, the system loss exceeds the gain at this stage. However, as the iterations proceed, both the gain and loss of the system increase progressively with the number of iterations. Before the 30-th iteration, the system gain consistently remains

TABLE I
PARAMETER SETTING

Parameter	Symbol	Value
Carrier frequency of uplink and downlink	f_1, f_2	31, 29 GHz
Wavelength of uplink and downlink	λ_1, λ_2	(0.97, 1.03) cm
BS Tx and UE Rx antenna element spacing	$d_{\text{BS}}^t, d_{\text{UE}}^r$	0.48 cm
BS Rx and UE Tx antenna element spacing	$d_{\text{BS}}^r, d_{\text{UE}}^t$	0.52 cm
Power ratio of BS and UE communication	$\beta_{\text{com}}, \gamma_{\text{com}}$	0.1
Power ratio of BS used for localization	β_{loc}	0.1
Power ratio of UE used for operation	γ_{work}	0.2
Maximum spectral efficiency	ζ_{max}	4.8 bps/Hz [37]
Phase noise of PLL	-	0.3 rad [38]
Antenna gain	$G(\theta, \phi)$	≤ 4.97 dBi [39]
RDA array size	M, N	40×40 [23]
Ambient temperature	T	295 K
Wave impedance	η	377Ω [33]
Path loss factor	\mathcal{L}	3 dB [40]
Link length	l	{3, 4, 5} m
Path loss exponent	α	2
Initial input power of BS	$\sum_{m=1}^M P_{\text{BS},m}^t(0)$	0.1 mW
Monte Carlo number	I	100

higher than the loss. After 30 iterations, both the gain and loss gradually stabilize and essentially cancel each other out. At this point, the system establishes resonance, the signal strength becomes stable, and a foundation is laid for subsequent communication and passive localization.

Fig. 5 illustrates the normalized distribution of spatial signal strength in the xoz-plane, comparing the downlink and uplink signal distributions during the initial transmission stage and after the system reaches a steady state.

From the Fig. 5 (a), it can be observed that during the first transmission of the downlink, the signal power emitted by the BS towards the UE exhibits a diffuse distribution, primarily concentrated near the BS. An effective directional transmission path has not yet formed, and most of the signal power is lost in space, resulting in low power reaching the UE and poor transmission efficiency. Fig. 5 (b) shows the spatial signal strength distribution of the uplink when the passive UE reflects a small amount of signal power received from the BS back along the original path through the RDAs. At this stage, the uplink transmission suffers from severe scattering and lacks strong directionality. As the iterations progress, the spatial electromagnetic field begins to self-replicate, eventually forming resonance. Fig. 5 (c) presents the spatial signal strength distribution of the downlink after the system has reached a steady state. It is evident that the signal power forms a highly directional and focused transmission path in space, reaching its maximum value along the straight-line region between the BS and the UE. Fig. 5 (d) shows the spatial signal strength distribution of the uplink after the system has achieved resonance. Compared to Fig. 5 (b), the signal strength distribution has significantly improved, with the signal power now highly focused along the straight-line region between the

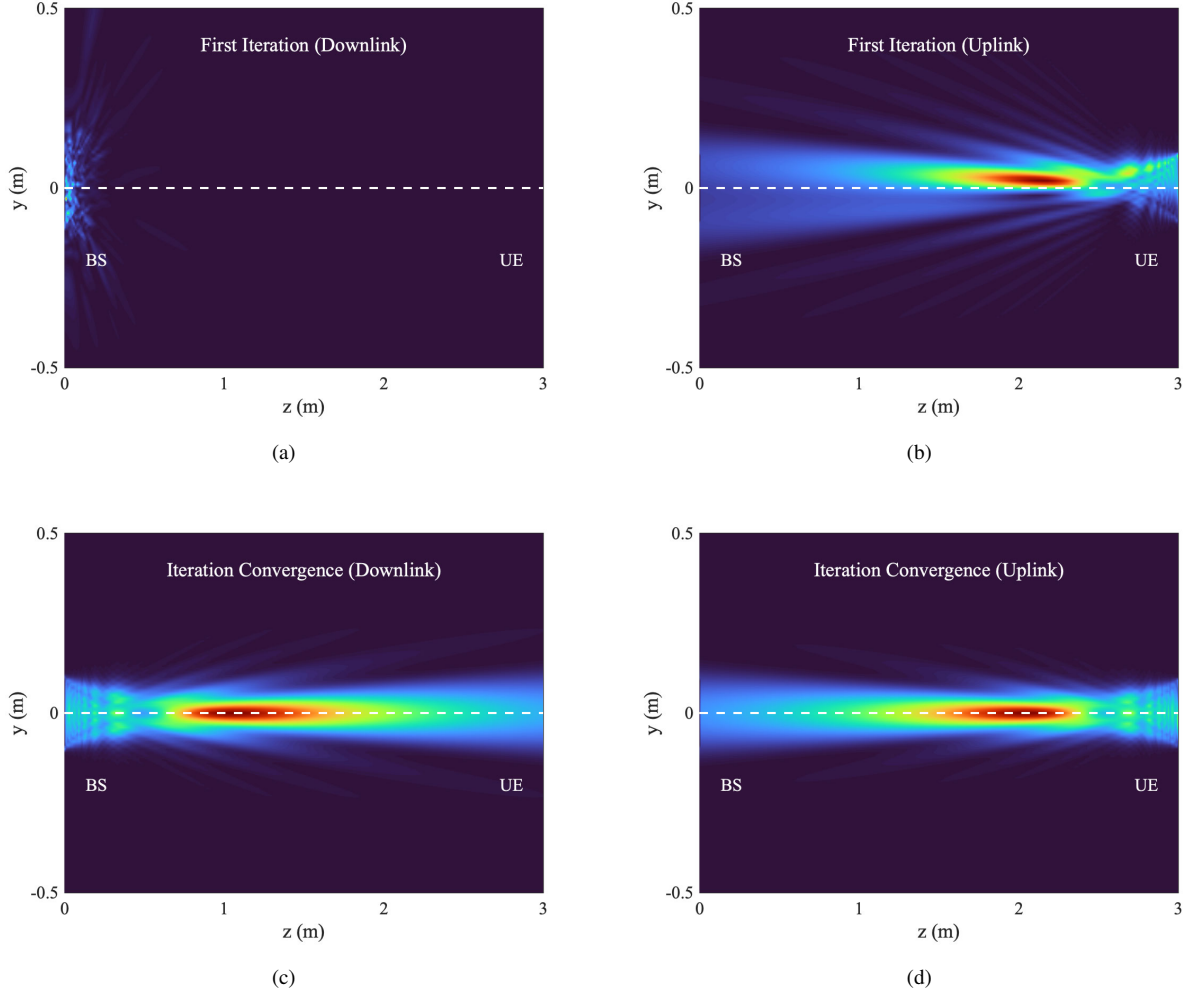


Fig. 5. Normalized distribution of spatial signal strength in xoz -plane. (a) Distribution of signal strength for the first transmission of the downlink; (b) The strength distribution of the first transmission signal on the uplink; (c) After the system reaches steady state, the distribution of downlink signal strength; (d) After the system reaches steady state, the distribution of uplink signal strength.

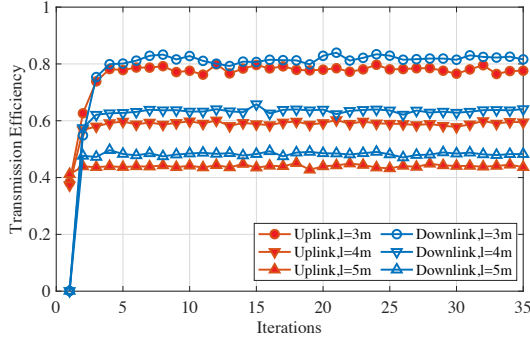
UE and the BS. This confirms that the system, through iterative optimization, gradually establishes a stable resonance path, enabling highly directional electromagnetic wave transmission. This result facilitates the realization of integrated passive communication and localization.

Fig. 6 illustrates the effects of the number of iterations and link length on the transmission efficiency and SNR of the RB-ISAC system. Fig. 6 (a) shows the variation in transmission efficiency with the number of iterations under different link lengths. The results reveal that as the number of iterations increases, the transmission efficiency gradually improves and eventually stabilizes. For short link lengths ($l = 3$ m), both the uplink and downlink transmission efficiencies converge to high levels near 0.8, demonstrating excellent transmission performance. However, for longer link lengths ($l = 4$ m and $l = 5$ m), the final converged transmission efficiencies are lower. In particular, at $l = 5$ m, the transmission efficiency is less than 0.5. This phenomenon highlights the significant impact of link length on transmission efficiency, where increased link length leads to greater signal attenuation and noise interference, thus

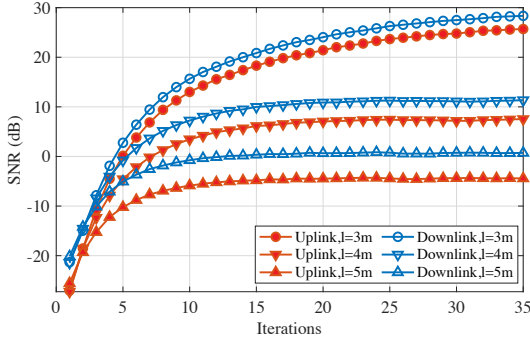
reducing overall transmission efficiency.

In Fig. 6 (b), we further explore the variation in SNR with the number of iterations under different link lengths. The simulation results indicate that SNR increases significantly during the initial iterations and gradually converges with further iterations. This is because, as iterations progress, the transmission efficiency of both the uplink and downlink continuously improves, resulting in an increase in the signal strength received by the BS and UE. However, for long-distance transmission, the signal strength gradually diminishes.

Fig. 7 depicts the relationship between SE and the number of iterations under different link lengths. The results show that for short links ($l = 3$ m), SE increases rapidly during the early iterations and converges to nearly 5 bps/Hz after about 15 iterations. For $l = 4$ m and $l = 5$ m, the rate of improvement in SE is slower, and the final converged values are lower. Notably, at $l = 5$ m, the SE converges to less than 1 bps/Hz. This decline is attributed to the reduction in SNR with increased link length, requiring more iterations to achieve optimal communication quality. This ensures that the RB-ISAC system can continuously

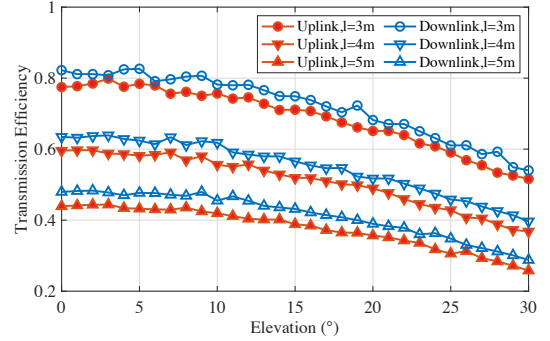


(a)

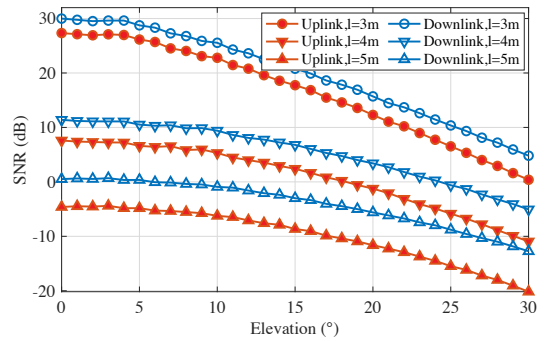


(b)

Fig. 6. System performance analysis with iteration times. (a) transmission efficiency analysis; (b) SNR analysis.



(a)



(b)

Fig. 8. System performance analysis with different elevation. (a) transmission efficiency analysis; (b) SNR analysis.

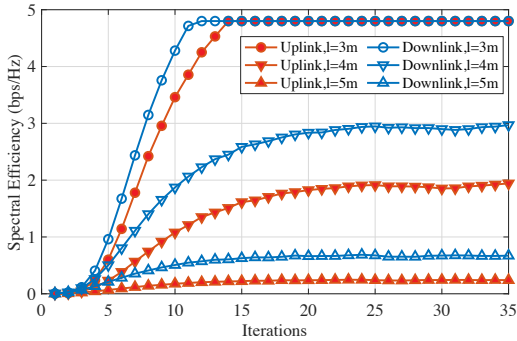


Fig. 7. Spectrum efficiency analysis with iteration times.

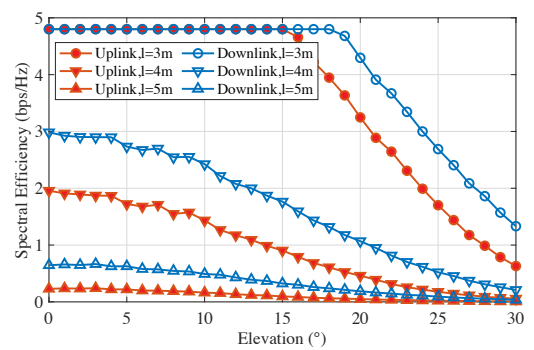


Fig. 9. Spectrum efficiency analysis with different elevation.

provide higher-quality communication services to the UE. In summary, it can be seen that the communication quality of RB-ISAC can be rapidly improved during the process of establishing resonance. In the next section, we provide a detailed analysis of the communication performance of the RB-ISAC system under different DOA conditions.

B. Communication Performance Analysis

In the RB-ISAC system, the elevation angle directly impacts antenna gain. Therefore, Fig. 8 illustrates the effects of elevation angle and link length on the transmission efficiency and SNR of the system.

Fig. 8 (a) shows the variation in transmission efficiency with elevation angle under different link lengths. It can be observed that for shorter link lengths (e.g., $l = 4$ m), the

system's transmission efficiency is highest, especially in lower elevation angle regions. This indicates that under short link lengths and ideal antenna alignment, the RB-ISAC system demonstrates exceptionally high robustness in communication. As the link length increases to $l = 4$ m and $l = 5$ m, the transmission efficiency decreases, and the influence of elevation angle becomes more pronounced.

In Fig. 8 (b), we further explore the relationship between SNR and elevation angle under different link lengths. Similarly, for short links ($l = 4$ m), the SNR remains high across the entire elevation angle range. This is because, in short-distance communication, signal attenuation is minimal, the signal power dominates, and the noise effect is negligible. However, for longer link lengths ($l = 4$ m and $l = 5$ m), SNR decreases significantly with increasing elevation angle, especially at high

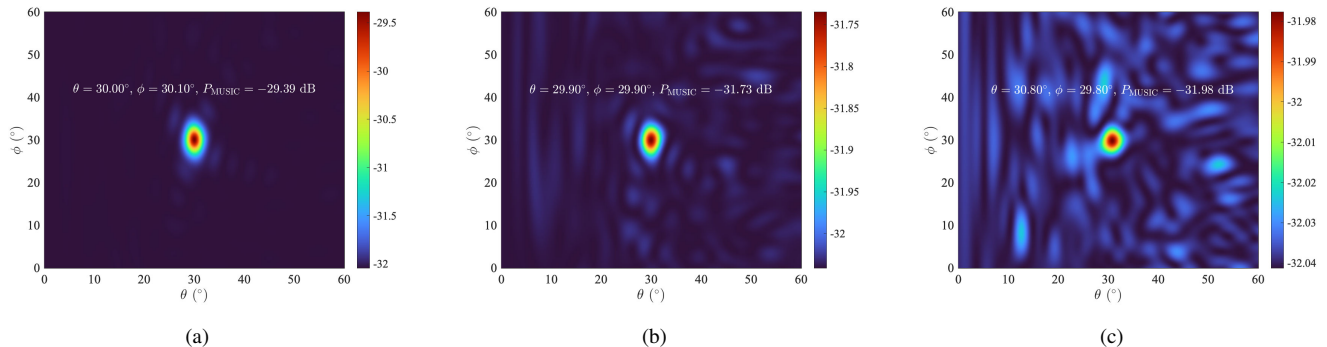


Fig. 10. The DOA estimation results of RB-ISAC system at different link lengths have true value of $\theta = \phi = 30^\circ$. (a) $l=3\text{m}$; (b) $l=4\text{m}$; (c) $l=5\text{m}$.

angles. Moreover, it can be observed that the downlink SNR decreases more slowly than the uplink, due to the effect of the power amplifier. This phenomenon highlights the nonlinear relationship between SNR and spatial angles, emphasizing the importance of beam alignment in maintaining high-quality communication.

In Fig. 9, we illustrate the SE variation with elevation angle under different link conditions. For short links ($l = 3\text{ m}$), the SE approaches the theoretical limit (5 bps/Hz) and is minimally affected by the elevation angle. However, as the link length increases, SE declines noticeably. In particular, at $l = 5\text{ m}$, this decline is more severe, exhibiting a sharp decay trend with increasing elevation angle. At high angles (e.g., 30°), the SE of long links approaches zero. This is because increased link length leads to greater transmission losses, significantly reducing the system's channel capacity.

In summary, these simulation results reveal that link length and elevation angle are two critical factors influencing system communication performance. Under short link conditions, the RB-ISAC system exhibits high robustness. These findings suggest that in practical deployments, it is essential to optimize the geometric configuration of the links. Particularly for long-distance and high-angle scenarios, RB-ISAC should incorporate beam self-alignment along with effective signal gain compensation techniques to enhance overall system performance.

C. Passive DOA Estimation Analysis

In Fig. 10, we conduct a simulation analysis of the DOA estimation performance of RB-ISAC using the MUSIC algorithm at different link lengths. In Fig. 10 (a), the spectral peaks are prominent and concentrated, indicating that the algorithm achieves high resolution and accuracy under near-distance conditions. This is attributed to the high SNR, which ensures stable estimation results without significant noise interference. As the link length increases to 4m (Fig. 10 (b)), the spectrum becomes less clear due to noise interference. The increased path loss from the greater link length leads to a reduction in SNR, and the spectral peak values also diminish. When the link length is further extended to 5m (Fig. 10 (c)), the received signal strength weakens further, and background noise intensifies. Consequently, the MUSIC algorithm's estimation

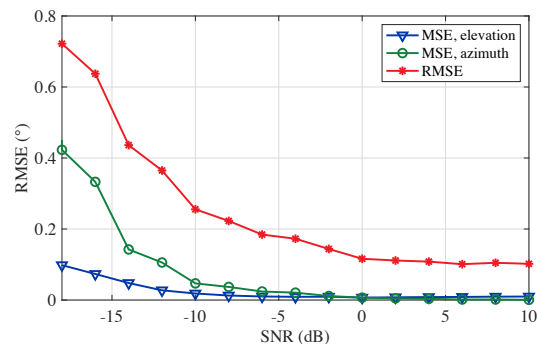


Fig. 11. The RMSE of RB-SLAC system in different SNR.

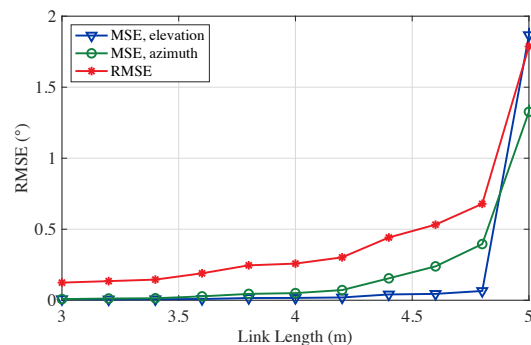


Fig. 12. The RMSE of RB-SLAC system in different link length.

accuracy and spectral peak resolution decline, resulting in the largest localization error.

In Fig. 11, we have demonstrated the distribution of root mean square error (RMSE) obtained through 100 Monte Carlo experiments. RMSE, as a crucial metric for evaluating the accuracy of model predictions, reflects the deviation between predicted values and actual values. It can be derived from the mean square error (MSE) of the elevation and azimuth angles [41], expressed as

$$\begin{aligned} \text{RMSE} &= \sqrt{\text{MSE}_\theta + \text{MSE}_\phi} \\ &= \sqrt{\frac{1}{I} \sum_{i=1}^I \{(\theta_i - \theta_0)^2 + (\phi_i - \phi_0)^2\}} \quad (35) \end{aligned}$$

where the θ_0 and ϕ_0 are the true values. From the figure, it is evident that as the SNR increases, the DOA estimation error decreases significantly due to the diminishing influence of noise. Notably, the RMSE of the elevation angle is consistently lower than that of the azimuth angle, indicating that the RB-ISAC system demonstrates higher sensitivity and accuracy in elevation angle estimation.

In Fig. 12, we show the RMSE performance of the RB-SLAC system at different link lengths. The elevation angle, azimuth angle, and overall RMSE were evaluated separately in the figure. From the Fig. 12, it can be seen that when the link length is between 3 m and 4.5 m, the RMSE remains relatively low and stable, indicating that the system can achieve high localization accuracy within this range. However, when the link length approached 5 m, the RMSE of all indicators shows a significant increase. This performance degradation is caused by signal attenuation, which has a negative impact on the accuracy of DOA estimation.

V. CONCLUSION

In this paper, we proposed a novel passive RB-ISAC system that utilized the self-alignment and power concentration characteristics of resonant beams for passive sensing and communication. By implementing signal recovery and enhancement mechanisms along with frequency adjustments, the system achieved closed-loop transmission of both uplink and downlink signals. Specifically, to address the interference caused by echoes in RF resonant localization systems, we have established a dual frequency resonant system using a PLL based RDA array in the mmWave band. Subsequently, we developed an electromagnetic wave circulation model for RB-ISAC, analyzed the conditions for resonance formation and channel characteristics, and performed DOA estimation based on the signals reflected back from UE received by the BS. Finally, simulations validated that the proposed system could achieve resonance after multiple iterations through effective compensation for signal propagation loss, enabling high-precision passive DOA estimation while supporting uplink and downlink communication. This approach simplified the beam control complexity of traditional MIMO-ISAC systems and reduced the computational load of the system.

REFERENCES

- [1] F. Liu, Y. Cui, C. Masouros, J. Xu, T. X. Han, Y. C. Eldar, and S. Buzzi, "Integrated sensing and communications: Toward dual-functional wireless networks for 6G and beyond," *IEEE J. Sel. Areas Commun.*, vol. 40, no. 6, pp. 1728–1767, 2022.
- [2] J. G. Andrews, S. Buzzi, W. Choi, S. V. Hanly, A. Lozano, A. C. Soong, and J. C. Zhang, "What will 5G be?" *IEEE J. Sel. Areas Commun.*, vol. 32, no. 6, pp. 1065–1082, 2014.
- [3] A. Conti, F. Morselli, Z. Liu, S. Bartoletti, S. Mazuelas, W. C. Lindsey, and M. Z. Win, "Location awareness in beyond 5G networks," *IEEE Commun. Mag.*, vol. 59, no. 11, pp. 22–27, 2021.

- [4] Z. Xiao and Y. Zeng, "An overview on integrated localization and communication towards 6G," *Sci. China Inf. Sci.*, vol. 65, no. 3, p. 131301, 2022.
- [5] W. Wang and W. Zhang, "Joint beam training and positioning for intelligent reflecting surfaces assisted millimeter wave communications," *IEEE Trans. Wireless Commun.*, vol. 20, no. 10, pp. 6282–6297, 2021.
- [6] J. Li, Y. Niu, H. Wu, B. Ai, S. Chen, Z. Feng, Z. Zhong, and N. Wang, "Mobility support for millimeter wave communications: Opportunities and challenges," *IEEE Commun. Surv. Tutor.*, vol. 24, no. 3, pp. 1816–1842, 2022.
- [7] M. Alsenwi, M. Abolhasan, and J. Lipman, "Intelligent and reliable millimeter wave communications for RIS-aided vehicular networks," *IEEE Trans. Intell. Transp. Syst.*, vol. 23, no. 11, pp. 21 582–21 592, 2022.
- [8] A. Ali, N. Gonzalez-Prelcic, R. W. Heath, and A. Ghosh, "Leveraging sensing at the infrastructure for mmwave communication," *IEEE Commun. Mag.*, vol. 58, no. 7, pp. 84–89, 2020.
- [9] A. Sesyuk, S. Ioannou, and M. Raspopoulos, "3D millimeter-wave indoor localization," in *2023 13th Int. Conf. Indoor Positioning Indoor Navig. (IPIN)*. IEEE, 2023, pp. 1–7.
- [10] M. Ruble and I. Güvenç, "Wireless localization for mmwave networks in urban environments," *EURASIP J. Adv. Signal Process.*, vol. 2018, pp. 1–19, 2018.
- [11] B. Zhou, A. Liu, and V. Lau, "Successive localization and beamforming in 5g mmwave MIMO communication systems," *IEEE Trans. Signal Process.*, vol. 67, no. 6, pp. 1620–1635, 2019.
- [12] Z. Aliyazicioglu, H. Hwang, M. Grice, and A. Yakovlev, "Sensitivity analysis for direction of arrival estimation using a Root-MUSIC algorithm," *Eng. Lett.*, vol. 16, no. 3, 2008.
- [13] P. Wang, J. Fang, X. Zeng, Z. Chen, and H. Li, "Low-complexity joint transceiver optimization for mmWave/THz MU-MIMO ISAC systems," *IEEE Internet Things J.*, 2024.
- [14] A. M. Elbir, K. V. Mishra, A. Abdallah, A. Celik, and A. M. Eltawil, "Spatial path index modulation in mmWave/THz band integrated sensing and communications," *IEEE Trans. Wireless Commun.*, 2024.
- [15] X. Cheng, D. Duan, S. Gao, and L. Yang, "Integrated sensing and communications (ISAC) for vehicular communication networks (VCN)," *IEEE Internet Things J.*, vol. 9, no. 23, pp. 23 441–23 451, 2022.
- [16] R. Zhang, Y. Zhang, R. Tang, H. Zhao, Q. Xiao, and C. Wang, "A joint UAV trajectory, user association, and beamforming design strategy for multi-UAV assisted ISAC systems," *IEEE Internet Things J.*, 2024.
- [17] Y.-N. R. Li, B. Gao, X. Zhang, and K. Huang, "Beam management in millimeter-wave communications for 5G and beyond," *IEEE Access*, vol. 8, pp. 13 282–13 293, 2020.
- [18] C. Qi, W. Ci, J. Zhang, and X. You, "Hybrid beamforming for millimeter wave mimo integrated sensing and communications," *IEEE Commun. Lett.*, vol. 26, no. 5, pp. 1136–1140, 2022.
- [19] M. Xiong, Q. Liu, S. Zhou, S. Han, and M. Liu, "Performance of a high power and capacity mobile SLIPT scheme," *IEEE Trans. Commun.*, vol. 70, no. 7, pp. 4717–4730, 2022.
- [20] M. Liu, Q. Jiang, M. Xu, and Q. Liu, "Passive location estimation via resonant beam," *IEEE Trans. Veh. Technol.*, vol. 72, no. 10, pp. 13 055–13 066, 2023.
- [21] W. Wang, Q. Zhang, H. Lin, M. Liu, X. Liang, and Q. Liu, "Wireless energy transmission channel modeling in resonant beam charging for IoT devices," *IEEE Internet Things J.*, vol. 6, no. 2, pp. 3976–3986, 2019.
- [22] H. Deng, S. Zhao, M. Liu, and Q. Liu, "Joint sensing and power transfer via distributed coupled-cavity lasers," *IEEE Internet Things J.*, 2023.
- [23] Y. Guo, Q. Jiang, M. Xu, W. Fang, Q. Liu, G. Yan, Q. Yang, and H. Lu, "Resonant beam enabled DoA estimation in passive positioning system," *IEEE Trans. Wireless Commun.*, vol. 23, no. 11, pp. 16 290–16 300, 2024.
- [24] Q. Jiang, M. Liu, M. Xu, W. Fang, M. Xiong, Q. Liu, and S. Zhou, "Self-alignment radio frequency resonant beam system for information and power transfer," *arXiv preprint arXiv:2411.10151*, 2024.
- [25] S. Xia, Q. Jiang, W. Fang, Q. Liu, S. Zhou, M. Liu, and M. Xiong, "Millimeter-wave resonant beam SWIPT," *IEEE Internet Things J.*, 2024.
- [26] X. Song, X. Li, X. Qin, and J. Xu, "Fully-passive versus semi-passive IRS-enabled sensing: Snr analysis," in *2023 IEEE Globecom Workshops (GC Wkshps)*. IEEE, 2023, pp. 1874–1879.
- [27] A. Winterstein, L. A. Greda, and A. Dreher, "A PLL-based retro-directive antenna system for communications with arbitrary frequency gaps," in *2015 9th Eur. Conf. Antennas Propag. (EuCAP)*. IEEE, 2015, pp. 1–5.
- [28] V. Fusco, C. B. Soo, and N. Buchanan, "Analysis and characterization of PLL-based retrodirective array," *IEEE Trans. Microw. Theory Tech.*, vol. 53, no. 2, pp. 730–738, 2005.

- [29] N. B. Buchanan, V. F. Fusco, and M. van der Vorst, "SATCOM retrodirective array," *IEEE Trans. Microw. Theory Tech.*, vol. 64, no. 5, pp. 1614–1621, 2016.
- [30] N. Buchanan, V. Fusco, and M. Van Der Vorst, "A high performance analogue retrodirective phase conjugation circuit with RX array factor combination ability," in *2011 IEEE MTT-S Int. Microw. Symp.* IEEE, 2011, pp. 1–4.
- [31] B. Friedlander, "Localization of signals in the near-field of an antenna array," *IEEE Trans. Signal Process.*, vol. 67, no. 15, pp. 3885–3893, 2019.
- [32] Y. Kang, X. Q. Lin, Y. Li, and B. Wang, "Dual-frequency retrodirective antenna array with wide dynamic range for wireless power transfer," *IEEE Antennas Wireless Propag. Lett.*, vol. 22, no. 2, pp. 427–431, 2022.
- [33] B. S. Guru and H. R. Hiziroglu, *Electromagnetic field theory fundamentals*. Cambridge Univ. Press, 2009.
- [34] H. Farès, B. Vrigneau, and O. Berder, "Green communication via harq protocols using message-passing decoder over AWGN channels," in *2015 IEEE Annu. Int. Symp. Pers. Indoor Mobile Radio Commun. (PIMRC)*. IEEE, 2015, pp. 197–201.
- [35] S. Kim, H.-W. Jo, J.-W. Kim, J.-I. Oh, J.-W. Yu, and B. Ahn, "Curved-retrodirective beamforming system to improve microwave power transmission efficiency in the Fresnel region," *IEEE Internet Things J.*, vol. 10, no. 17, pp. 15 012–15 024, 2023.
- [36] S. Dutta, C. N. Barati, D. Ramirez, A. Dhananjay, J. F. Buckwalter, and S. Rangan, "A case for digital beamforming at mmwave," *IEEE Trans. Wireless Commun.*, vol. 19, no. 2, pp. 756–770, 2019.
- [37] M. R. Akdeniz, Y. Liu, M. K. Samimi, S. Sun, S. Rangan, T. S. Rappaport, and E. Erkip, "Millimeter wave channel modeling and cellular capacity evaluation," *IEEE J. Sel. Areas Commun.*, vol. 32, no. 6, pp. 1164–1179, 2014.
- [38] J.-Y. Lee, S.-H. Lee, H. Kim, and H.-K. Yu, "A 28.5–32-GHz fast settling multichannel PLL synthesizer for 60-GHz WPAN radio," *IEEE Trans. Microw. Theory Tech.*, vol. 56, no. 5, pp. 1234–1246, 2008.
- [39] C. A. Balanis, *Antenna theory: analysis and design*. John Wiley & Sons, 2016.
- [40] S. H. A. Shah, S. Aditya, and S. Rangan, "Power-efficient beam tracking during connected mode drx in mmwave and sub-thz systems," *IEEE J. Sel. Areas Commun.*, vol. 39, no. 6, pp. 1711–1724, 2021.
- [41] A. R. Carballeira, F. A. de Figueiredo, and J. M. C. Brito, "Simultaneous estimation of azimuth and elevation angles using a decision tree-based method," *Sensors*, vol. 23, no. 16, p. 7114, 2023.